Insights on the surface chemistry of BiVO4 photoelectrodes and the role of Al overlayers on its water oxidation activity

Applied Catalysis A, General 605 (2020) 117796

Contents lists available at ScienceDirect

Applied Catalysis A, General

journal homepage: www.elsevier.com/locate/apcata

Insights on the surface chemistry of $BiVO_4$ photoelectrodes and the role of Al overlayers on its water oxidation activity

Kristine Rodulfo Tolod[a,b,*], Tapish Saboo[b], Simelys Hernández[a,*], Hilmar Guzmán[a,c], Micaela Castellino[a], Rowshanak Irani[d], Peter Bogdanoff[d], Fatwa F. Abdi[d], Elsje Alessandra Quadrelli[b], Nunzio Russo[a]

[a] Department of Applied Science and Technology, Politecnico di Torino, Corso Duca degli Abruzzi, 10129 Turin, Italy
[b] Université de Lyon, Institut de Chimie de Lyon, UMR 5265 – CNRS – Université Lyon 1, ESCPE Lyon, Laboratoire de Chimie, Catalyse, Polymères et Procédés (C2P2), Equipe Chimie Organométallique de Surface, 43, Bd du 11 Novembre 1918, F-69616 Villeurbanne, France
[c] Center for Sustainable Future Technologies, Istituto Italiano di Tecnologia @ Polito, Via Livorno, 60, 10144, Turin, Italy
[d] Institute for Solar Fuels, Helmholtz-Zentrum Berlin für Materialien und Energie GmbH, Hahn-Meitner-Platz 1, Berlin 14109, Germany

ARTICLE INFO

Keywords:
$BiVO_4$
Al overlayer
Passivation layer
Photoanode
Surface chemistry
Water splitting
Artificial photosynthesis
Surface organometallic chemistry

ABSTRACT

Bismuth vanadate ($BiVO_4$) has surface states that give rise to defect levels that mediate electron-hole recombination. In order to minimize the inefficiencies, an ultrathin Al overlayer was deposited on the $BiVO_4$ electrodes. A 54 % improvement on the photocurrent density was obtained using the Al-modified $BiVO_4$ electrode, accompanied by a 15 % increase in stability over 7.5 h of continuous irradiation. Moreover, surface capacitance measurements showed that the Al overlayer was indeed passivating the surface states. We also shed light on the deposition of an Al overlayer on the surface of $BiVO_4$, by investigating the process on model $BiVO_4$ powders. This study presents useful, previously unreported information about the surface chemistry of $BiVO_4$ based on experimental methods and gives unique insights on the characterization of the $BiVO_4$ surface. The existence of surface reactive sites on $BiVO_4$ was confirmed and quantified (1.5 reactive sites/nm^2) via chemical titration.

1. Introduction

Photoelectrochemical water splitting is a sustainable means to produce H_2, which can serve as a clean source of fuel. In this process, liquid water is split into its gaseous H_2 and O_2 components (H_2O + photons → H_2 + ½ O_2), via the use of photo-activated semiconductor catalysts, by utilizing the photons coming from the sun and using them to directly convert the solar energy into chemical energy. To be able to split water into hydrogen and oxygen efficiently and sustainably, the photo-voltage must be sufficient, there should be an appropriate band alignment in the semiconductor, a substantial absorption of the solar spectrum and an efficient and fast transport of charges between the semiconductor and the electrolyte [1,2]. In addition, the semiconductor must be stable and cost-effective. The search for suitable materials that satisfy these requirements is the focus of the current ongoing studies in photoelectrochemistry and photocatalysis because no single material can fulfil all these requirements; trade-offs exist among the light-harvesting ability, the charge transport and charge transfer processes, and the catalyst's influence in the kinetics of the reaction.

The bottleneck in the photoelectrochemical water splitting process is the water oxidation reaction in the photoanode [3,4], which is the focus of this study. Metal oxides [5,6] are preferred as photoanodes, mainly because of their resistance to oxidizing conditions [2]. Compared to other metal oxides like hematite (α-Fe_2O_3) and WO_3, bismuth vanadate ($BiVO_4$) is preferred because its conduction band edge position nearly coincides with the thermodynamic hydrogen evolution potential [7,8], which is instrumental in promoting an earlier photocurrent onset and enabling the generation of higher photocurrents in the low bias region [9]. It also has a relatively low band gap energy (2.4–2.5 eV), which makes it readily absorb visible light [10,11]. The theoretical maximum photocurrent density of $BiVO_4$ is 7.5 mA/cm^2, which translates to a maximum of 9% of solar-to-hydrogen (STH) efficiency [12,13] assuming all of the sunlight photons with energies greater than 2.4 eV are absorbed by the semiconductor and have contributed to the photocurrent.

However, solid semiconductors such as $BiVO_4$ have surface states that are associated with the abrupt termination and discontinuity of the solid crystal at the crystal boundary. As a result, the electronic band

* Corresponding authors at: Department of Applied Science and Technology, Politecnico di Torino, Corso Duca degli Abruzzi, 10129 Turin, Italy.
E-mail addresses: kristine.tolod@polito.it (K.R. Tolod), simelys.hernandez@polito.it (S. Hernández).

https://doi.org/10.1016/j.apcata.2020.117796
Received 10 August 2020; Accepted 15 August 2020
Available online 19 August 2020

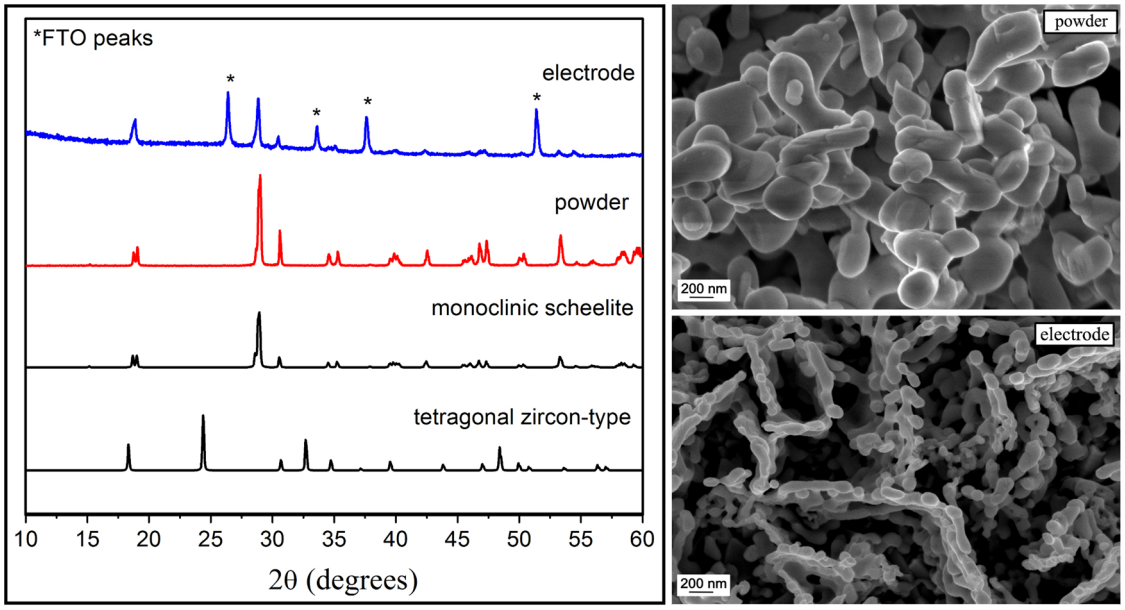

Fig. 1. XRD (left) and FESEM (right) images of bare $BiVO_4$ powder and thin-film electrode. The reference XRD spectra of monoclinic scheelite and tetragonal zircon-type structures of $BiVO_4$ are shown for comparison in the bottom of the left image.

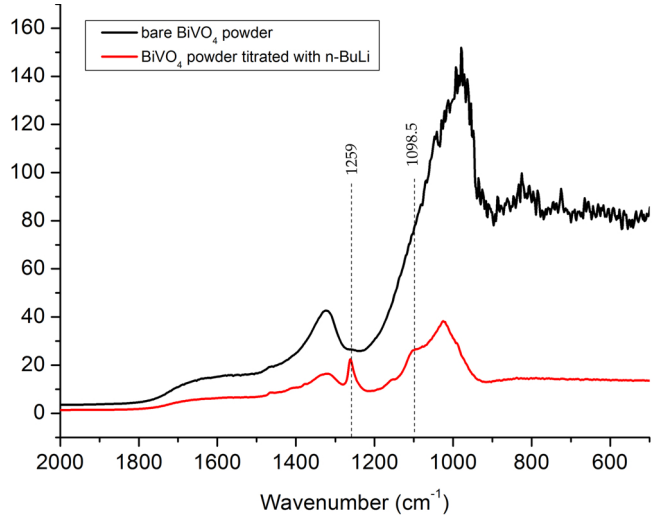

Fig. 2. FTIR spectra of bare $BiVO_4$ and $BiVO_4$ titrated with n-BuLi.

structure is quite different from the bulk, as characterized by dangling bonds [14]. These surface states have a modified band structure that may give rise to defect energy levels, which may lie within the previously forbidden band gap region away from the band edges. These can mediate electron-hole recombination via the Shockley-Read-Hall mechanism wherein the electron from the conduction band can move towards the defect level, release the energy as photon or phonons, and eventually relax into the valence band, annihilating a hole in the process.

In photoelectrochemical systems, passivation layers have been used as an effective strategy to improve the charge separation and transfer processes across semiconductor–liquid interfaces. These thin layers can reduce the charge recombination at surface states, increase the water oxidation reaction kinetics, and protect the semiconductor from chemical corrosion. These layers are < 100 nm thick but quite often, only 1–2 nm are used to allow the charge transfer by means of tunneling. Passivation layers can be fabricated through the use of several relatively scalable techniques such as atomic layer deposition (ALD), spin-coating, electrochemical deposition, sputtering, electron beam evaporation, floating transfer and dip-casting [15–17].

Al_2O_3 has been used as a passivation layer for both p- and n-type silicon solar cells. Al_2O_3 is a wide band gap material (5–9 eV) which exists in different crystalline forms, exhibits low leakage current, and has a modest value of dielectric constant [18]. It finds its use as a gate dielectric in metal oxide semiconductor (MOS) transistors and is a suitable insulator for various electronic applications. In the photovoltaic field, the importance and crucial impact of surface recombination to the resulting photoactivity of conventional semiconductors has been very much highlighted. Al_2O_3 as a passivation layer is unique because it combines the effect of both chemical and field effect passivation by providing hydrogen to the Si interface during the post-deposition thermal treatments and also for having a very high density of negative charges located near the interface [19]. However, the use of Al_2O_3 as a passivation layer for $BiVO_4$ photoanodes has not been largely investigated. To date, only one paper reported the use of Al_2O_3 as a passivation layer for $BiVO_4$ [20]. It was shown that adding an Al overlayer with an optimal thickness can double the photocurrent density, however, the nature of the specific surface interactions between the Al overlayer and the $BiVO_4$ remains to be studied.

This study presents novel findings about the use of ultrathin overlayers of Al to enhance the photoactivity of $BiVO_4$. Moreover, an organometallic chemistry approach was used to study this very important surface as well as to introduce surface modifications that could help improve the photoactivity and the stability of this material.

2. Experimental

2.1. Materials and methods

2.1.1. Synthesis procedures

A full description of materials and methods used for the synthesis of both $BiVO_4$ powders and films is reported in the Supporting Information (SI, sections S1 and S2). Briefly, the $BiVO_4$ powder was synthesised by hydrothermal method employing a solution of bismuth nitrate and ammonium metavanadate as precursors, under acidic media (pH = 0), in an autoclave at 180 °C for 12 h, according to a previous published procedure [21]. The crystalline $BiVO_4$ powder was obtained after calcination under air atmosphere at 400 °C for 2 h. The $BiVO_4$ films were synthesised based on a previously optimized

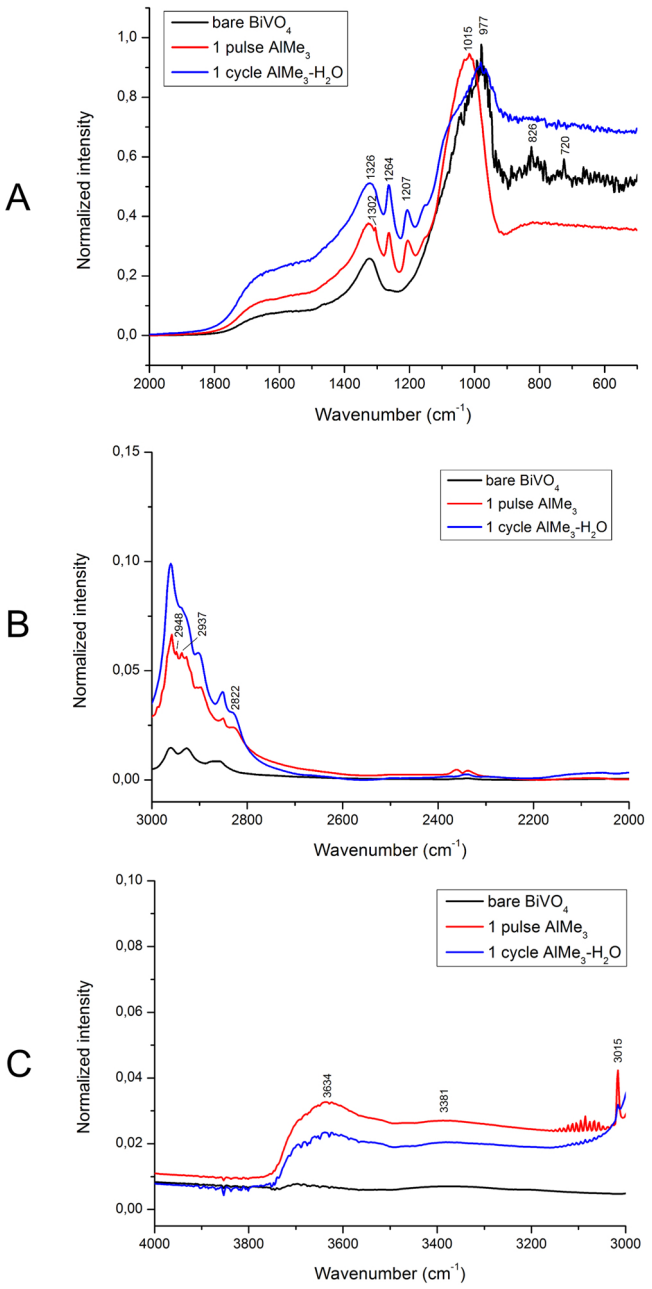

Fig. 3. FTIR Spectra of dehydroxylated bare $BiVO_4$ powder, $BiVO_4$ powder with 1 pulse of $AlMe_3$ and 1 cycle $AlMe_3$-H_2O at (A) 2000-500 cm^{-1} wavenumbers, (B) 3000-2000 cm^{-1} wavenumber, (C) 4000-3000 cm^{-1} wavenumber.

electrodeposition method [22]. In brief, BiOI was electrodeposited on F-doped Tin oxide (FTO)/glass substrate by using a solution of bismuth nitrate, potassium iodide, p-benzoquinone and ethanol. The BiOI film was subsequently transformed in $BiVO_4$ by addition of a solution of vanadyl acetylacetonate in dimethyl sulfoxide and calcination under air atmosphere at 425 °C for 2 h. The photoelectrode area is of 1 cm^2. The $BiVO_4$ powders and thin films were modified by the addition of Al_2O_3 with the procedure described in the SI (sections S1.4 and S2.3, respectively). In particular, the $BiVO_4$ films with different amounts (or cycles) of deposited Al_2O_3 were investigated.

2.1.2. Materials characterization

A Merlin Zeiss Field Emission – Scanning Electron Microscope (FESEM) equipped with an Energy Dispersive X-ray Spectroscopy System (EDS) was used to study the morphology of the samples. The XRD spectra were obtained by using an X'Pert Phillips diffractometer under Cu Kα radiation (λ = 1.5418 Å) set at 40 kV and 40 mA. N_2 adsorption and desorption isotherms were obtained at 77 K on a degassed sample using Belsorp-Max from BEL-JAPAN. The DRIFTS spectra were obtained using a Nicolet 6700-FT spectrometer. Gas chromatography (GC) measurements were determined using a HP 5890 gas chromatograph equipped with a flame ionization detector (FID) and a KCl/Al_2O_3 on fused silica column (50 m × 0.32 mm). UV–vis absorption spectra of $BiVO_4$ films were measured using a Perkin–Elmer Lambda 950 double-beam spectrometer equipped with an integrating sphere. X-ray photoelectron spectroscopy (XPS) measurements were performed) with a monochromatic Al Kα radiation (hν = 1486.74 eV), in order to determine the surface composition of the $BiVO_4$ electrodes and their stability after the photoelectrochemical tests. Bare $BiVO_4$ samples were first analysed by using a PHI 5000 Versa Probe (Physical Electronics) system. Subsequently, a SPECS FOCUS 500 monochromator and a hemispherical electron analyzer (SPECS PHOIBOS 100) were employed to further analyse the bare and Al-modified $BiVO_4$ samples before and after testing. The binding energies for all spectra were calibrated with respect to the adventitious carbon C 1s peak at 284.5 eV. Peak fitting was done using XPSPEAK software with a Shirley background subtraction.

2.1.3. Photoelectrochemical (PEC) characterization

A Pt coil counter electrode (CE), an Ag/AgCl (3 M KCl) reference electrode (RE), and the $BiVO_4$ photoanode as the working electrode (WE), were assembled in a single-compartment quartz cell containing a 0.1 M NaPi solution (pH 7). The simulated sunlight irradiation was from a Newport 450 W Xe lamp source that was equipped with an AM 1.5 G filter (intensity of 100 mW/cm^2). Illumination was performed under back illumination on a geometric area of 1 cm^2, which corresponds to the entire deposited area of the electrode.

The PEC tests were performed using a BioLogic VSP 300 potentiostat. Linear sweep voltammetry (LSV) in continuous and chopped light modes and chronoamperometry (CA) were performed to characterize the photoactivity of the electrodes. Linear sweep voltammetry was performed at the potential range of -0.3 V to 1 V *vs.* Ag/AgCl, using a scan rate of 10 mV/s. Chronoamperometry was done at 0.61 V *vs.* Ag/AgCl. The following Nernst equation was used to convert the potentials versus the Ag/AgCl (3 M KCl) reference electrode to RHE (NHE at pH = 0):

$$E_{RHE} = E_{\frac{Ag}{AgCl}} + 0.059pH + E^{o}_{\frac{Ag}{AgCl}} \left(E^{o}_{\frac{Ag}{AgCl}} = +0.199\,V \right) \quad (1)$$

MS-SPEIS (Mott Schottky-Staircase Potentio Electrochemical Impedance Spectroscopy) analysis was done under an applied potential of -0.8 V to 1 V (*vs.* Ag/AgCl), and a frequency of 7.5 kHz. Mott-Schottky plots were used to extrapolate the flat band potentials (E_{fb}) and donor densities (N_D) of the photoanodes, according to the equation:

$$\frac{1}{C^2} = \frac{2}{\varepsilon\varepsilon_o A^2 e N_D}\left(E - E_{fb} - \frac{k_B T}{e}\right) \quad (2)$$

where C is the interfacial capacitance, ε is the dielectric constant of the semiconductor, ε_o is the permittivity of free space, A is the area of the interfacial capacitance, N_D is the donor density, E is the applied potential, E_{fb} is the flat-band potential, k_B is the Boltzmann's constant, T is the temperature and e is the electronic charge. A plot of $\frac{1}{C^2}A^2$ versus the potential yields a linear region.

Charge transport and transfer properties of the photoanodes were studied using electrochemical impedance spectroscopy (EIS), at frequencies from 0.1 Hz to 0.5 MHz, a potential of 0.61 V *vs.* Ag/AgCl, under simulated sunlight illumination.

Monochromatic photocurrents (i_{ph}) of $BiVO_4$ films were measured under the illumination of a Xe lamp source (Oriel, 300 W) coupled with a grating monochromator (Acton SpectraPro 2150i). A long-pass filter

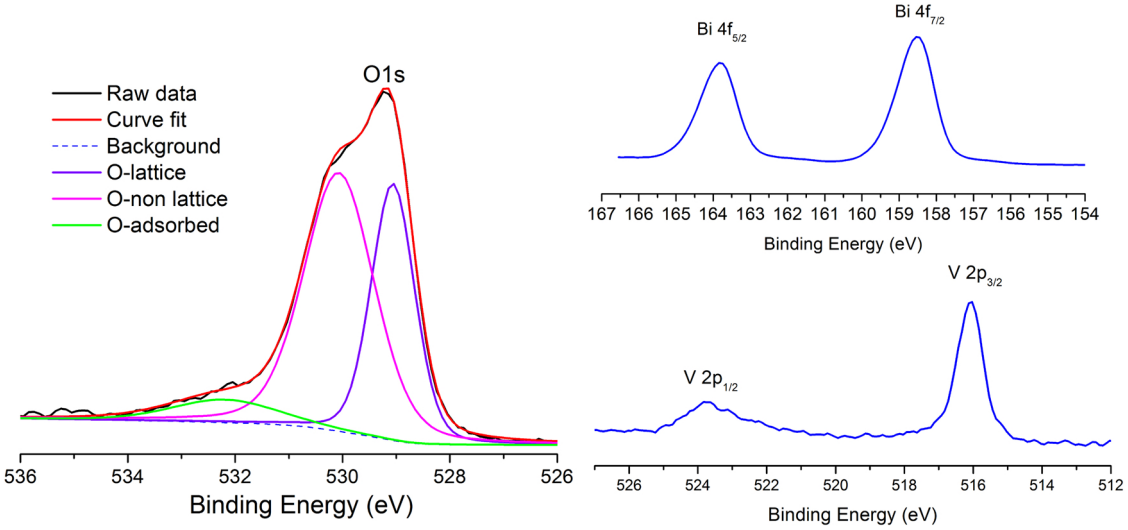

Fig. 4. O1s, Bi 4f and V2p XPS spectra for bare $BiVO_4$ electrode.

(Schott, 3 mm thick) was placed between the monochromator and the sample in order to remove any second-order diffracted light. The optical power of lights reaching the films (P) was measured using a calibrated photodiode (Ophir, PD300R-UV with Nova II controller). An EG&G Princeton Applied Research 283 potentiostat was used to apply the bias potential. An Ag/AgCl (saturated KCl, XR300 Radiometer Analytical) and a platinum wire were used as the reference and counter electrode, respectively. Incident photon-to-current conversion efficiency (IPCE) values for each wavelength (λ) were calculated using the following formula:

$$\mathrm{IPCE}(\lambda) = \frac{1240 \times i_{ph}(\mathrm{mA})}{P(\mathrm{mW}) \times \lambda(\mathrm{nm})} \times 100\% \quad (3)$$

For O_2 detection, differential electrochemical mass spectrometry measurements were performed using a setup described in details elsewhere [23,24]. Signal calibration was performed by measuring the O_2 signal vs. current for a Pt sheet. The Faradaic efficiency (FE) was then calculated using the following equation, under the assumption that the Pt sheet has 100 % Faradaic efficiency for the O_2 evolution reaction:

$$\mathrm{FE} = \frac{O_2 \text{ signal from sample}}{O_2 \text{ signal from Pt sheet}} \quad (4)$$

Finally, rapid scan voltammetry was performed. A constant potential of 1.5 V vs Ag/AgCl (2.1 V vs RHE) was applied for 2 min as a conditioning step, followed by a quick potential sweep to -0.2 V vs Ag/AgCl (0.4 V vs RHE) with a scan rate of 1 V/s. Comparison of the curves with and without conditioning yields the surface capacitance (C) through the equation $C = (J_{\text{with cond}} - J_{\text{w/out cond}})/\text{scan rate}$.

3. Results and discussions

3.1. Morphology and structure

$BiVO_4$ has three main crystal forms: monoclinic scheelite, tetragonal zircon-type and tetragonal scheelite. There is an irreversible transition from the tetragonal zircon-type to the monoclinic scheelite structure that occurs at 400–500 °C. At 255 °C, another reversible transition also occurs between the monoclinic-scheelite and the tetragonal scheelite structures. Furthermore, mechanical grinding at room temperature can also irreversibly transform the tetragonal structure into a monoclinic structure [25]. Among these three crystal structures, the monoclinic scheelite structure is the most commonly used for photocatalysis because of its higher photoactivity compared to the other structures [26]. We prepared two different form of samples: $BiVO_4$ powders that were synthesized hydrothermally and $BiVO_4$ thin-film electrodes prepared via electrodeposition. The reader is referred to the Supporting Information (S1 and S2) for the detailed synthesis procedures. The XRD spectra in Fig. 1 showed that both the $BiVO_4$ electrode and the $BiVO_4$ powder manifested the monoclinic scheelite structure (JCPDS No. 14-0688, space group: I2/a, a = 5.195, b = 11.701, c = 5.092, β = 90.38°), which is evident from the peak splitting at the 2θ values of 18.5° and 35°. No traces of other phases were observed in these diffraction patterns, which points out the suitability of the chosen synthesis methods towards the monoclinic phase of $BiVO_4$. For an easy comparison, the XRD reference spectra of $BiVO_4$ with monoclinic scheelite and tetragonal zircon-type structures are also shown in the Fig. 1.

From the FESEM images in Fig. 1, it is evident that there were very distinct differences between the resulting morphologies of the $BiVO_4$ powder and the thin-film electrode. The $BiVO_4$ powder morphology consists of a more agglomerated and compact structure that is made up of big grain sizes, while the thin film electrode showed a more porous structure that is not agglomerated, and with smaller grains. In agreement with this, the crystallite sizes for the powder and the thin film electrode, which were determined from the X-ray diffraction data, are found to be 320 and 112 nm, respectively. More intense peaks were observed from the powder samples because of the higher amount of material present than in the thin-film electrode. From FESEM-EDS, the ratio of Bi/V for each of the samples was both found to be 1, which means that the 1:1 ratio of Bi: V is well-maintained in the bulk for both samples. Nitrogen adsorption-desorption isotherms were used for the BET surface area measurements for the $BiVO_4$ powder, which revealed a rather low surface area of 2–4 m^2/g.

3.2. $BiVO_4$ powder

The nature of the $BiVO_4$ surface was studied by the chemical titration of the $BiVO_4$ powder with n-butyllithium (n-BuLi), a carbanionic reagent, typically used in surface organometallic chemistry for the titration of surface acid protons (see SI, section S1.3, for more details). The n-BuLi is known to react with the surface hydroxyls and chemisorbed water of inorganic oxides [27] to yield butane (C4H10) that can be quantified using a gas chromatograph (GC).

From the n-BuLi reaction, 8.8 μmol of butane gas (C4H10) was evolved when contacted with the thermally-treated, dehydroxylated $BiVO_4$. If one extrapolated such chemical reaction to exclusive reaction with surface reactive sites, the result translates to 1.5 surface reactive sites/nm2 on the $BiVO_4$ surface. The reader is referred to the SI (section

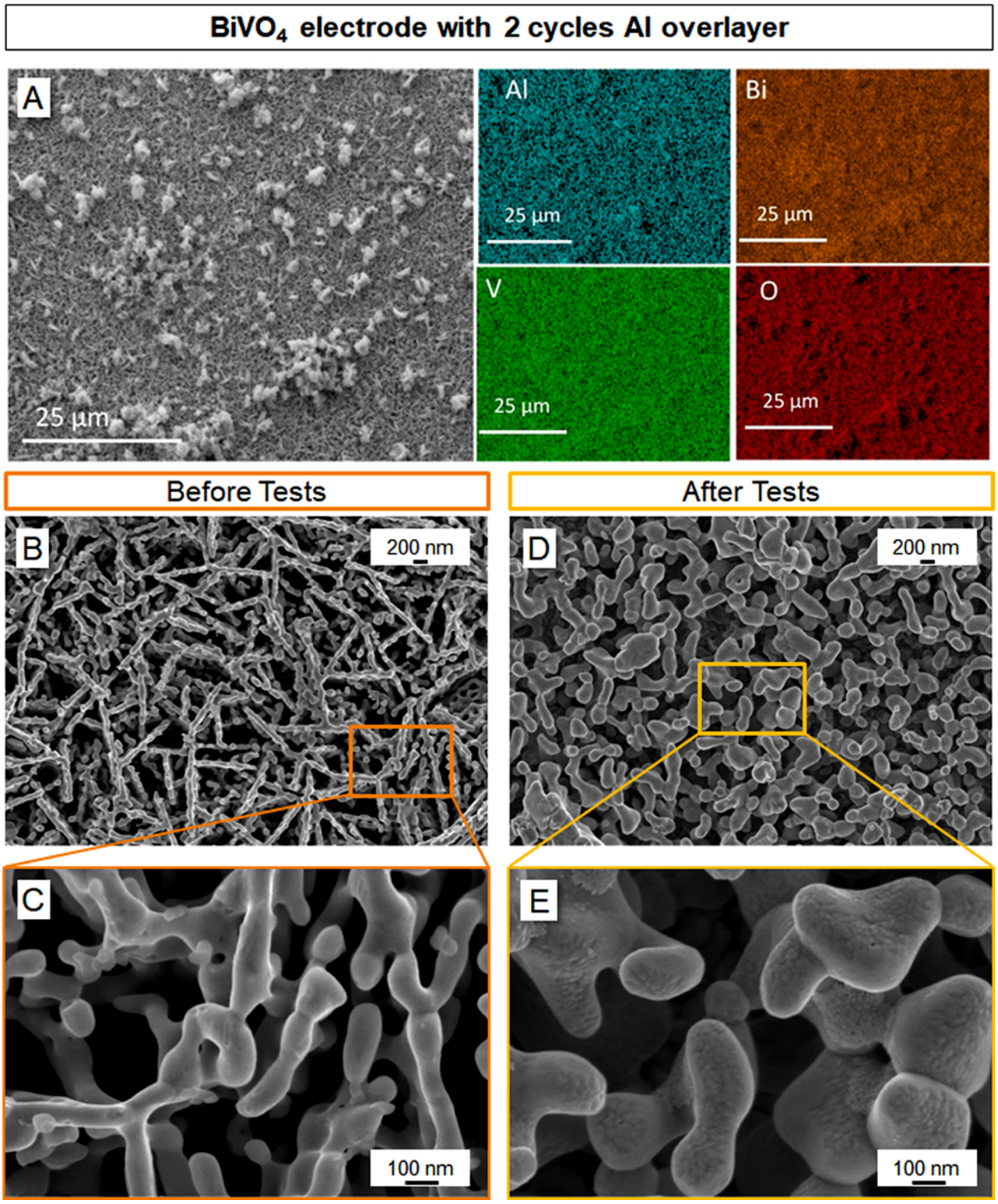

Fig. 5. FESEM-EDS analyses of Al-modified $BiVO_4$ electrode made by 2 cycles: Low magnification FESEM image and EDS maps of Al, Bi, V and O elements on the fresh electrode (A); FESEM images before (B, C) and after (D, E) photo-electrochemical water oxidation tests in 0.1 M NaPi buffer.

S3) for the gas chromatography calculations. In a study by Starr et al. [28], it was shown that single crystal $BiVO_4$ exhibited the presence of surface hydroxyl groups, however, there is no evidence in literature that confirms their presence in polycrystalline structures such as $BiVO_4$ powders.

The IR spectra of the pristine $BiVO_4$ powder (black line) and the titrated $BiVO_4$ powder (red line) in the 500–2000 cm-1 region is shown in Fig. 2. The $BiVO_4$ powder titrated with n-BuLi showed two distinct IR bands in the 1098.5 cm-1 and 1259 cm-1 regions. This preliminary data necessitates further studies to characterize the surface chemical species and to see if hydroxyl to O-Li + titration with concomitant alkane stoichiometric release is the dominant surface reactivity. As of now, the 1.5 OH/nm^2 can be considered as an upper boundary estimate of the hydroxyl population on the $BiVO_4$ surface. To the best of our

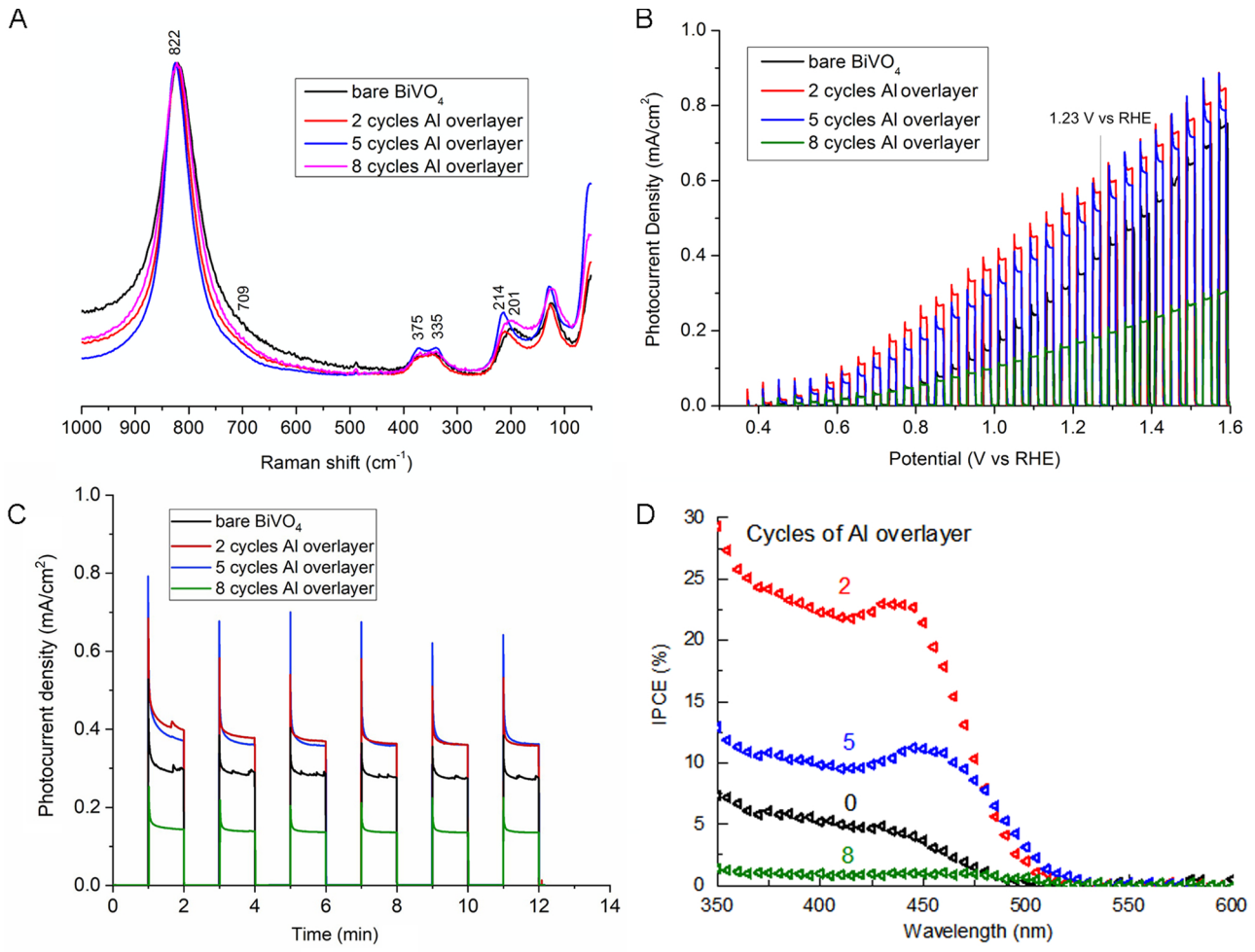

Fig. 6. (A) Raman spectra of bare and Al-modified $BiVO_4$ electrodes. PEC water oxidation tests of bare and Al-modified $BiVO_4$: (B) LSV plots under chopped light (scan rate: 10 mV/s), (C) chronoamperometries under chopped light, (D) IPCE spectra and (D) Raman spectra. Tests were made with 0.1 M Na-Pi buffer pH 7.

knowledge, this quantification of the reactive groups in $BiVO_4$ surface has not been previously reported in literature.

The addition of an Al overlayer was also performed on $BiVO_4$ powder in order to model the $BiVO_4$-Al interface formed on the photoanode. Such modeling on the powder's surface, which has a 10^4-fold larger surface area than that of the thin film electrode (ca. 2 m^2/g for powder vs. few cm^2/g for the electrode), allows to use millimolar range routine characterization techniques (such as DRIFT IR, elemental analysis by combustion, GC analysis of the gas phase), thus, giving molecular-level insight to the surface processes, which would be more difficult to harness directly from the electrode surface [29].

The accepted simplified ALD-mechanism for Al_2O_3 growth on OH–terminated surfaces is shown below, with * denoting the surface species [30].

$$Al\text{-}OH^* + Al(CH_3)_3 \rightarrow Al\text{-}O\text{-}Al(CH_3)_2^* + CH_4 \quad (A)$$

$$Al\text{-}OH_3^{*+} H_2O \rightarrow Al\text{-}OH^* + CH_4 \quad (B)$$

When the reaction is performed in a sequential manner, i.e. A-B-A-B-A-B…, a controlled layer-by-layer growth of Al_2O_3 is achieved. However, to the best of our knowledge, the mechanism of the growth of an Al overlayer on $BiVO_4$ has not been investigated to date. We have earlier established and quantified the presence of reactive sites on the $BiVO_4$ surface, and we have hypothesized that some OH groups can serve as initial binding sites for the Al atoms as indicated in sequence A. Consequently, the growth of the Al overlayer in an A-B-A-B-A-B sequential manner should also be possible for $BiVO_4$.

Fig. 3 shows the IR spectra of (i) vacuum pre-treated pristine $BiVO_4$, (ii) $BiVO_4$ powder with 1 pulse of $AlMe_3$, and (iii) after reaction with H_2O. The starting bare $BiVO_4$, i.e., before the 1st pulse of $AlMe_3$, is characterized by peaks at 720 cm^{-1}, 826 cm^{-1}, and 977 cm^{-1} which correspond to V–O waging, symmetric, and asymmetric vibrations, respectively [31]. Peaks associated with O–H stretching vibrations are expected in 3374 cm^{-1} and 3700 cm^{-1} wavenumbers, although for the case of $BiVO_4$ it is not readily seen in the IR spectra.

Upon addition of the first pulse of $AlMe_3$, the presence of the $AlCH_3$* surface species was confirmed by the presence of the diagnostic ν(C–H) stretching vibrations seen at 2822–2948 cm^{-1}. The 3015, 1207, 1015, 1264 and 1302 cm^{-1} peaks are yet unassigned. The subsequent H_2O pulse resulted to a broad O-H band at 3400 cm^{-1} in agreement with expected AlO-H stretching vibrations from AlOH* surface species in the 3600 cm^{-1} region. The contribution to this band from OH vibration mode of physiosorbed water molecules should be limited, due to the vacuum treatment step undergone by the sample between the water addition and the IR analysis.

Upon water addition on the Al-Me terminated surface (see reaction B above), the volatiles were condensed, analyzed and quantified by gas chromatography. In agreement with reaction B, methane was detected in the gas phase. The quantification of methane translated to 1.2 CH_4 evolved per reactive group titrated on the initial surface. This result is in the correct order of magnitude for the simplified growth mechanism proposed for ALD cycles to alumina and is also compatible with the possible formation of dipodal surface species $[(-O)_2AlMe]$.

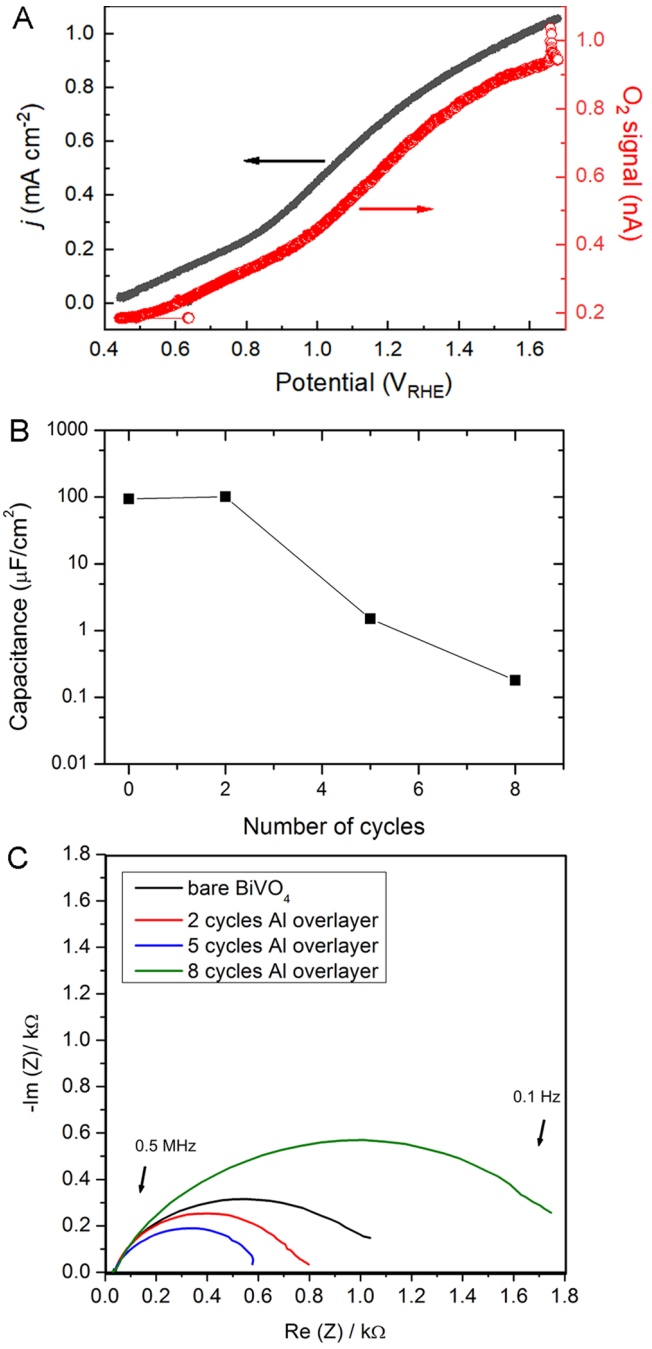

Fig. 7. (A) Measurement of O_2 signal detected simultaneously during linear sweep voltammetry on 2 cycles Al-modified electrode. (B) Surface capacitance and (C) Nyquist impedance plots for bare and Al-modified $BiVO_4$.

3.3. $BiVO_4$ thin-film electrode

The chemical composition of the $BiVO_4$ thin film electrodes was determined by XRD, XPS, FESEM-EDS and Raman analyses.

The high resolution XPS spectra for Bi4f, V2p, and O1 s binding energy regions are shown in Fig. 4. In agreement with the XRD data (see Section 3.1), the thin-film photoelectrodes manifest the spin-orbit splitting for both the $Bi4f_{7/2}$ and $Bi4f_{5/2}$, and the $V2p_{3/2}$ and $V2p_{1/2}$, that are in good agreement with those reported in literature for monoclinic-scheelite structure of $BiVO_4$ [32]. Also, it is noteworthy that the $Bi4f_{7/2}$ and $Bi4f_{5/2}$ peaks appear in the binding energy region (158.5 eV and 163.8 eV, respectively) that is much higher than that of metallic Bi, i.e. 156.8 eV and 162.2 eV [32], respectively. These Bi4f peaks indicate the presence of Bi occurring mainly as Bi^{3+} species in the surface of the electrodes. Meanwhile, the $V2p_{3/2}$ and $V2p_{1/2}$ peaks at 516.1 eV and 523.7 eV, respectively, are characteristic of V occurring mainly as V^{4+} species on the surface of the photoanode. This is different from the bulk V species, which have a +5 oxidation state, as implied by EDS measurements and by earlier studies by us with depth profile XPS measurements [22]. The reduction of V^{5+} to V^{4+} on the surface of the $BiVO_4$ electrode induces oxygen vacancies that directly impact the electronic structure of the monoclinic scheelite $BiVO_4$. In fact, these oxygen vacancies has been observed from the O 1s spectra, the deconvolution of which yielded lattice oxygen at 529.2 eV, non-lattice oxygen at 530.3 eV, and chemisorbed or dissociated oxygen from water molecules at 532.0 eV [32–36]. The non-lattice oxygen refers to oxygen-deficient regions which might be populated with OH groups in order to correct the charge balance.

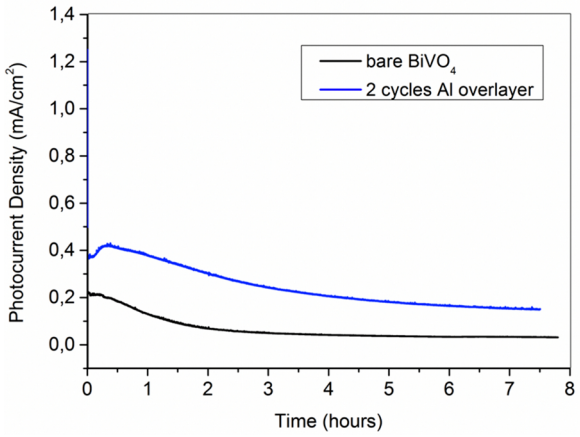

Fig. 8. Stability test (chronoamperometry) plot for 2 cycles Al and bare $BiVO_4$.

Furthermore, surface Bi/V atomic ratios revealed a Bi-rich surface for the $BiVO_4$ electrode before PEC tests (Bi/V: 2.3), while EDS measurements show a Bi/V ratio of 1 in the bulk. The Bi-rich surface of the $BiVO_4$ is a consequence of the segregation phenomena that has been observed for Bi-containing oxides, wherein the oxygen segregates to the surface, depleting the subsurface of oxygen, and leading to Bi-O surface terminations [37].

Upon Al-overlayer deposition, XPS investigation was also performed, and the spectra are shown in Figure S6. As expected, Al peak is clearly seen for the $BiVO_4$ sample that is modified with Al-overlayer deposition, whereas none can be observed for the bare $BiVO_4$. No change is observed for the V 2p peaks upon Al-overlayer deposition, but additional peaks at higher binding energies can be observed in the Bi 4f spectra. These are assigned to Bi^{5+}, as also reported in the literature [38,39]. This shows that the Al-overlayer deposition slightly oxidize the surface of the $BiVO_4$.

As a representative of the Al-modified samples, in Fig. 5A is shown a low magnification FESEM image with an EDS map of Al, Bi, V and O elements in the $BiVO_4$ thin-film with 2 cycles of Al overlayer, which demonstrate an uniform coverage of FTO/glass substrate with the $BiVO_4$ film and an homogeneous deposition of Al on it, even at a low number of deposition cycles. Other elements (i.e. Si and Sn, not shown) were also visible in the EDS analyses due to the FTO/glass substrate. As shown in Fig. 5B and C, the nanostructured porous morphology of the $BiVO_4$ particles remains unmodified and, as found in the bare $BiVO_4$, a Bi/V ratio of 1 was also observed in the Al-modified samples, confirming the no modification of the chemical composition of $BiVO_4$ after the Al deposition process.

The Raman spectra of bare and Al-modified $BiVO_4$ thin film electrodes are shown in Fig. 6A. The most intense band at 822 cm^{-1} is assigned to the V–O stretching mode and the weak shoulder at 709 cm^{-1} is assigned to antisymmetric V–O stretching. The bands at 375 cm^{-1} and

335 cm^{-1} correspond to the symmetric and antisymmetric bending of VO_4 tetrahedra. There was a slight difference observed at the 201–214 cm^{-1} bands, but these are ascribed to the external mode of $BiVO_4$, which is not exactly structural in nature [40]. Therefore, based on the Raman spectra, it can be also confirmed that the Al overlayer did not induce structural modifications on the $BiVO_4$. This result is also supported by the UV–Vis absorption analysis shown in Fig. S3 in the SI. Only minor differences are observed in the absorption spectra of all the bare $BiVO_4$ and Al-modified $BiVO_4$ samples (Fig. S3A), which is within the sample-to-sample variation. From these absorption spectra, Tauc analyses were performed in order to determine the bandgaps. Tauc plots for direct and indirect bandgap analyses are shown in Figure S3B and C, respectively, where only very little changes of bandgaps are observed (2,48 and 2,41 ± 0.01 eV, respectively). Overall, as expected, the Al overlayer does not affect the bulk structural and optical properties of $BiVO_4$.

The effect of varying the number of cycles in the ALD-like deposition method on the photoactivity of the $BiVO_4$ thin film electrodes was investigated. Fig. 6B and C shows the linear sweep voltammetry and chronoamperometry curves under chopped light conditions for all the samples modified with Al, as compared with that of the bare $BiVO_4$ thin film electrode. Indeed, for very few pulses of $AlMe_3$-H_2O cycles, the formation of alumina oxide cannot be inferred. All curves manifested the initial current spikes appearing readily when the light source was turned on, which eventually dampened, which suggests the occurrence of fast electron-hole recombination. For the bare $BiVO_4$ sample, a photocurrent density of 0.35 mA/cm^2 at 1.23 V vs RHE was achieved. It can be clearly seen from the same figure that an improvement in photocurrent density values was achieved with 2 cycles and 5 cycles of Al deposition, yielding 0.54 mA/cm^2 and 0.49 mA/cm^2 at 1.23 V vs RHE, respectively, in the LSV curves. Under CA tests at 1.23 V vs RHE, the photocurrents of these two samples stabilized at a bit lower and similar value of 0.38 mA/cm^2. However, lower photocurrent density was observed when the number of Al-deposition cycles was increased to 8. The influence of Al-deposition cycles to the incident photon-to-current conversion efficiency (IPCE) was also investigated and the resulting curves for the different samples under back-side illumination are shown in Fig. 6D. The IPCE increases from the bare $BiVO_4$ sample to that with 2 cycles Al deposition, and it decreases again for higher number of Al deposition cycles. The differences between samples are rather larger than those observed from the LSV curves. The reason for this may be related to the instability of the films, which will be discussed later in the manuscript. Nevertheless, the overall trend qualitatively agrees with the LSV and CA measurements.

It is noteworthy that the reaction temperature used in the ALD-like deposition of the Al overlayer on the $BiVO_4$ surface, which yielded the better performance is low enough at 60 °C, which is not commonly demonstrated in typical ALD processes involving Al_2O_3, commonly performed at 125–500 °C [30].

To confirm that the higher photocurrent values of the Al-modified $BiVO_4$ electrodes are mainly due to water oxidation, we measured the O_2 generated by the highest performing Al-modified samples (i.e. with 2 cycles) using differential electrochemical mass spectrometry (DEMS) (see experimental section for measurement details). Fig. 7A shows a linear sweep voltammetry curve, directly compared with the O_2 signal simultaneously measured with DEMS. Both curves correspond well with each other, suggesting that the O_2 generation can be correlated with the photocurrent. Indeed, by using the same system but under chronoamperometry condition, the Faradaic efficiency for O_2 evolution was determined to be 100.0 ± 0.6 % at 1.0 V vs. RHE. All photocurrents can therefore be attributed to the water oxidation reaction.

In order to verify if the Al overlayer is indeed passivating the surface states in the $BiVO_4$ electrode surface, rapid scan voltammetry was performed to determine the surface capacitance of the electrodes. As shown in Fig. 7B, the surface capacitance decreases by orders of magnitude with increasing number of cycles of Al, in agreement with passivating surface states that serve as charge recombination sites. This is important because the photocurrent of $BiVO_4$ has been reported to be limited more by surface recombination than the charge transfer [41].

Meanwhile, the Nyquist impedance plot is shown in Fig. 7C. The charge transfer resistance, which was indicated by the diameter of the arc, is seen to be highest for the 8 cycles Al electrode (green arc), and greater than that of bare $BiVO_4$ (black arc). This is consistent with the trend observed for the photocurrent density, where it was seen that the bare $BiVO_4$ performed better than the 8 cycles Al overlayer. Therefore, the thickest layer of Al overlayer contributed in slowing down the transfer of holes on the $BiVO_4$-electrolyte interface. Also, it can be seen from Fig. 7C, that the 2 cycles Al overlayer (red arc) and the 5 cycles Al overlayer (blue arc) have lower charge transfer resistances than the bare $BiVO_4$, thus, both having higher photocurrent density relative to the bare $BiVO_4$. However, between these 2 electrodes, it turned out that the 5 cycles Al has a lower charge transfer resistance than the 2 cycles Al, which was the opposite behaviour of the observed photocurrent density. It appears that the higher photocurrent density of the 2 cycles Al electrode is explained by the donor densities as derived from the Mott-Schottky plots (shown in Figure S4 in the SI), wherein the 2 cycles Al electrode manifested a donor density of 1.49×10^{20} cm^{-3}, while the 5 cycles Al electrode has a lower donor density of 1.16×10^{20} cm^{-3}. A higher donor density can improve the PEC response by raising the Fermi level, which creates more band bending that enhances electric field in the space charge layer, thus, lowering the electron-hole recombination. Second, it enhances the electrical conductivity of the photoanode, thus, improving the charge transport properties within the material. Moreover, the onset potentials of these electrodes were almost equal at 0.39 V, 0.37 V, 0.38 V, and 0.37 V vs RHE, for bare $BiVO_4$, 2 cycles Al, 5 cycles Al, and 8 cycles Al, respectively.

The 2 cycles Al electrode, which exhibited the best photocurrent density, was subjected to a stability test along with the bare $BiVO_4$ electrode. The result of the stability test is shown in Fig. 8. The bare $BiVO_4$ (black line) showed an 85 % decay in photocurrent density after 7.5 h, while the 2 cycles Al (blue line) electrode showed 59.6 % decay. To understand the reason of such decay in the performance, post-reaction FESEM-EDS and XPS analyses were performed. Fig. 5D and E show the FESEM images of the 2 cycles Al modified sample after testing. An increase of the $BiVO_4$ particles size and rearrangement of the porous structure of the film after the PEC test are observed. The same behavior was also noticed in the bare $BiVO_4$ film (see Figs. S5, SI); however, uncoated regions of the FTO substrate clearly appeared after the 7.5 h of operation in the bare $BiVO_4$ film (see Figure S5E, SI), while the Al-modified film was already preserved from this point of view. From EDS analyses it was observed a Bi-enrichment of the films: the Bi/V ratio increased from 1.0 to 1.2 and 1.1, in the bare $BiVO_4$ and the 2 cycles Al-modified electrode, respectively, which can be explained by the dissolution of V atoms from the $BiVO_4$ surface during the PEC tests [42]. Indeed, the Bi/V ratio from XPS analysis for the bare $BiVO_4$ slightly increases from 2.3 (vide supra) to 2.8 after PEC measurement. In addition, Bi atoms on the surface of the bare $BiVO_4$ sample become partially oxidized to Bi^{5+} ([Bi^{5+}] increased from 0 to ~20 %, see Fig. S7A), indicating that the photocurrent decay may be related to an oxidative photo-corrosion process. In contrast, although the Bi atoms are already partially oxidized to begin with in the 2 cycles Al-modified sample, PEC measurement only slightly oxidizes the surface further ([Bi^{5+}] slightly increased from 23 to 29 %, see Fig. S7B). Instead, the instability observed in the Al-modified $BiVO_4$ may be related to the detachment of Al, as observed from the disappearance of peak in the Al 2p core level spectra (see Fig. S7C). Further investigation on better adhesion of Al on the $BiVO_4$ surface is therefore needed in order to extend the stability.

Overall, although the stability of the $BiVO_4$ photoanode clearly remains an issue, it was demonstrated here that the presence of an Al overlayer on the $BiVO_4$ surface arrested some of the photo-corrosion and reduced the photocurrent decay by at least 15 %.

4. Conclusion

In order to minimize the inefficiencies due to electron-hole recombination and passivate the surface states, ultrathin Al oxo/hydroxyls overlayers were deposited onto the $BiVO_4$ thin film electrodes in an ALD-like manner (alternating pulses of trimethyl aluminum and water). This was also performed in order to protect the $BiVO_4$ surface from photocorrosion and increase its stability. A photocurrent density of 0.54 mA/cm^2 at 1.23 V vs RHE was obtained for the 2 cycles Al overlayer - $BiVO_4$ electrode, which was a 54 % improvement from the bare $BiVO_4$ that demonstrated a photocurrent density of 0.35 mA/cm^2 at 1.23 V vs RHE. A 15% increase in stability of the 2 cycles Al overlayer-$BiVO_4$ electrode was also observed over 7.5 h of continuous irradiation. Finally, through surface capacitance measurements, it was shown that the Al overlayer was indeed passivating the surface states of the $BiVO_4$ electrodes.

Chemical insight into the nature of the Al-modified $BiVO_4$ surface was also gained by studying the larger surface area $BiVO_4$ powder, used as a model of the photoanode. Chemical titration of the $BiVO_4$ powder with n-BuLi led to the evolution of butane (1.5 molecule/nm^2 of $BiVO_4$ surface), thus highlighting the existence of surface reactive groups on $BiVO_4$, whose chemical nature has not yet been defined. If the presence of surface hydroxyls, postulated elsewhere in the literature, is confirmed, this work suggests a maximum of 1.5 of such reactive site/nm^2 on $BiVO_4$. Such surface site reacts with $AlMe_3$ to yield surface alkyls, which can be hydrolyzed by a further pulse of water and concomitant methane release (1.2 CH_4 molecules released by the reactive group of the initial surface). This work on model powder $BiVO_4$ confirms that chemically reasonably well-behaved ALD–like half-cycles of $AlMe_3$ and H_2O can be alternated on $BiVO_4$ surfaces, thus providing a molecular model for the useful chemical modification reported herein for the thin film $BiVO_4$ photoanodes.

Declaration of interests

The authors declare that they have no known competing financial interests or personal relationships that could have appeared to influence the work reported in this paper.

Declaration of Competing Interest

The authors report no declarations of interest.

Acknowledgments

The authors thank the EACEA Erasmus+ SINCHEM Grant FPA 2013-0037 for the financial support. Part of the work described in this paper has been conducted within the project SUNCOCHEM. This project has received funding from the European Union's Horizon 2020 Research and Innovation Action programme under the Grant Agreement No 862192. From Politecnico di Torino, we acknowledge Mauro Raimondo for the FESEM measurements and Enrico Sartoretti for the assistance in Raman spectra interpretation. The support of CNRS, Université de Lyon 1 and CPE Lyon Sustainable chair is also gratefully acknowledged. We thank Christian Höhn for his assitance in the XPS measurement.

Appendix A. Supplementary data

Supplementary material related to this article can be found, in the online version, at doi:https://doi.org/10.1016/j.apcata.2020.117796.

References

[1] Z. Chen, H.N. Dinh, E. Miller, Photoelectrochemical Water Splitting Standards, Experimental Methods, and Protocols, (2013).
[2] M.G. Walter, E.L. Warren, J.R. McKone, S.W. Boettcher, Q. Mi, E.A. Santori, N.S. Lewis, Chem. Rev. (Washington, DC, United States) 110 (2010) 6446–6473.
[3] J.K. Hurst, Science (80-.) 328 (2010) 315–316.
[4] M. Grätzel, J. Moser 5 (2001) 589–644.
[5] A. Harriman, I.J. Pickering, J.M. Thomas, P.A. Christensen, J. Chem. SOC. Furuduy Trans. I 84 (1988) 2795–2806.
[6] J. Kiwi, M. Grätzel, Nature 281 (1979) 657–658.
[7] A. Kudo, Keiko Omori, H. Kato, (1999) 11459–11467.
[8] Y. Park, K.J. McDonald, K.-S. Choi, Chem. Soc. Rev. (2013) 2321–2337.
[9] T.W. Kim, Y. Ping, G.A. Galli, K.-S. Choi, Nat. Commun. 6 (2015) 8769.
[10] A. Kudo, K. Ueda, H. Kato, I. Mikami, Catal. Lett. 53 (1998) 229–230.
[11] D.J. Payne, M.D.M. Robinson, R.G. Egdell, A. Walsh, J. McNulty, K.E. Smith, L.F.J. Piper, Appl. Phys. Lett. 98 (2011) 46–49.
[12] S. Hu, C. Xiang, S. Haussener, A.D. Berger, N.S. Lewis, Energy Environ. Sci. 6 (2013) 2984–2993.
[13] F.F. Abdi, N. Firet, R. vandeKrol, ChemCatChem 5 (2013) 490–496.
[14] R.S. Bonilla, B. Hoex, P. Hamer, P.R. Wilshaw, Phys. Status Solidi A 214 (2017).
[15] L. Steier, I. Herraiz-cardona, S. Gimenez, F. Fabregat-santiago, J. Bisquert, S.D. Tilley, M. Grätzel, (2014).
[16] R. van de Krol, M. Grätzel, Photoelectrochemical Hydrogen Production, (2012).
[17] K. Tolod, S. Hernández, N. Russo, Catalysts 7 (2017) 13.
[18] E.O. Filatova, A.S. Konashuk, J. Phys. Chem. C 119 (2015) 20755–20761.
[19] G. Dingemans, W. Beyer, M.C.M. Van De Sanden, W.M.M. Kessels, 152106 (2012) 1–4.
[20] G. Chang, D.W.Y. Zhang, A. Aldalbahi, Nucl. Sci. Tech. (2016) 2–7.
[21] S.M. Thalluri, C. Martinez Suarez, S. Hernández, S. Bensaid, G. Saracco, N. Russo, Chem. Eng. J. 245 (2014) 124–132.
[22] K.R. Tolod, S. Hernández, M. Castellino, F.A. Deorsola, E. Davarpanah, N. Russo, Int. J. Hydrogen Energy 45 (2020) 605–618.
[23] F. Wang, W. Septina, A. Chemseddine, F.F. Abdi, D. Friedrich, P. Bogdanoff, R. Van De Krol, S.D. Tilley, S.P. Berglund, J. Am. Chem. Soc. 139 (2017) 15094–15103.
[24] R. Irani, P. Plate, C. Höhn, P. Bogdanoff, M. Wollgarten, K. Höflich, R. Van De Krol, F.F. Abdi, J. Mater. Chem. A 8 (2020) 5508–5516.
[25] A. Bhattacharya, K. Mallick, A. Hartridge, Mater. Lett. 30 (1997) 7–13.
[26] C. Martinez Suarez, S. Hernández, N. Russo, Appl. Catal. A Gen. 504 (2015) 158–170.
[27] C. Copéret, A. Comas-Vives, M.P. Conley, D.P. Estes, A. Fedorov, V. Mougel, H. Nagae, F. Nunez-Zarur, P.A. Zhizhko, Chem. Rev. 116 (2016) 323–421.
[28] D.E. Starr, M. Favaro, F.F. Abdi, H. Bluhm, E.J. Crumlin, R. van de Krol, J. Electron Spectros. Relat. Phenomena 221 (2017) 106–115.
[29] S. Cadot, O. Renault, M. Frégnaux, D. Rouchon, E. Nolot, K. Szeto, C. Thieuleux, L. Veyre, H. Okuno, F. Martin, E.A. Quadrelli, Nanoscale 9 (2017) 538–546.
[30] M.D. Groner, F.H. Fabreguette, J.W. Elam, S.M. George, (2004) 639–645.
[31] Z. Zhao, Z. Li, Z. Zou, RSC Adv. 1 (2011) 874–883.
[32] L.H. Dall'Antonia, N.R. de Tacconi, W. Chanmanee, H. Timmaji, N. Myung, K. Rajeshwar, Electrochem. Solid-State Lett. 13 (2010) D29.
[33] S. Wang, P. Chen, Y. Bai, J.H. Yun, G. Liu, L. Wang, Adv. Mater. 30 (2018) 1–7.
[34] J. Wu, Y. Chen, L. Pan, P. Wang, Y. Cui, D. Kong, L. Wang, X. Zhang, J. Zou, Appl. Catal. B Environ. 221 (2018) 187–195.
[35] S. Bai, Q. Li, J. Han, X. Yang, X. Shu, J. Sun, L. Sun, R. Luo, D. Li, A. Chen, Int. J. Hydrogen Energy 44 (2019) 24642–24652.
[36] H. Bai, P. Guan, K. Qu, W. Fan, F. Wang, D. Xu, J. Ding, W. Shi, Int. J. Hydrogen Energy 44 (2019) 28184–28193.
[37] D. Passerone, R. Erni, (2015).
[38] R.P. Antony, T. Baikie, S.Y. Chiam, Y. Ren, R.R. Prabhakar, S.K. Batabyal, S.C.J. Loo, J. Barber, L.H. Wong, Appl. Catal. A Gen. 526 (2016) 21–27.
[39] G. Zhang, L. Cai, Y. Zhang, Y. Wei, Chem. – A Eur. J. 24 (2018) 7434–7444.
[40] B.J. Yu, A. Kudo, (2006) 2163–2169.
[41] C. Zachäus, F.F. Abdi, L.M. Peter, R. Van De Krol, Chem. Sci. 8 (2017) 3712–3719.
[42] K. Sayama, A. Nomura, T. Arai, T. Sugita, R. Abe, T. Oi, Y. Iwasaki, Y. Abe, H. Sugihara, J. Phys. Chem. B 3 (2006) 11352–11360.